THE JOURNAL OF PHYSICAL CHEMISTRY C
A JOURNAL OF THE AMERICAN CHEMICAL SOCIETY

pubs.acs.org/JPCC

Article

Structural Dynamics of a Novel Pseudohalide Perovskite $Cs_2Pb(SeCN)_2Br_2$ Investigated with Nonlinear Infrared Spectroscopy

Xiangyu Xing, Jiayi Li, John P. Breen, Hemamala I. Karunadasa,* and Michael D. Fayer*

Cite This: https://doi.org/10.1021/acs.jpcc.3c02251

Read Online

ACCESS | Metrics & More | Article Recommendations | Supporting Information

ABSTRACT: Layered halide perovskites are candidates for applications, including solar cells, light-emitting diodes, and photodetectors, because of their diverse photophysical properties. Interplay between charge carriers and structural dynamics underlies the properties of perovskites. Here we report the first selenocyanate-based two-dimensional (2D) perovskite, $Cs_2Pb(SeCN)_2Br_2$. We investigate the lattice dynamics of this novel perovskite using ultrafast nonlinear infrared experiments. The CN stretching mode is used as the vibrational probe. It has a long vibrational lifetime, providing an extensive observational time window. The CN stretch of $Cs_2Pb(SeCN)_2Br_2$ has a much longer lifetime than the structurally analogous $Cs_2Pb(SCN)_2Br_2$, as a result of differences in vibrational energy relaxation pathways. Two-dimensional infrared spectroscopy was used to measure the homogeneous and inhomogeneous broadening of the CN absorption line. The results demonstrate that there is inhomogeneous broadening and spectral diffusion, i.e., inhomogeneous lattice structures undergo structural fluctuations. It is shown that the spectral diffusion has a constant component, which likely arises from permanent inhomogeneity of crystallites that compose the spin-coated thin films, e.g., from lattice strains. In comparison to $Cs_2Pb(SCN)_2Br_2$, $Cs_2Pb(SeCN)_2Br_2$ displays more inhomogeneous broadening and less homogeneous broadening, which is caused by coupling to phonons, and the spectral diffusion is approximately a factor of two slower. Analysis of the angular range of librational motions of the $SeCN^-$, measured with polarization-selective pump−probe spectroscopy, provides the librational angular well potential energy, which is lower than that of the $Cs_2Pb(SCN)_2Br_2$. Comparison of the SeCN- and SCN-containing 2D perovskites provides information on the effects of chalcogen substitution on lattice dynamics.

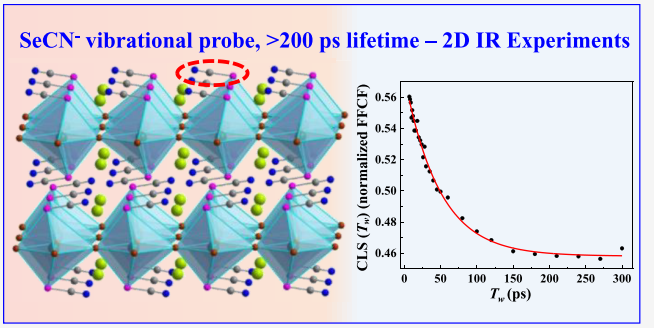

1. INTRODUCTION

Two-dimensional (2D) layered perovskites have been employed for various optoelectronic technologies owing to their photophysical properties and inexpensive syntheses.[1−7] The general formula of 2D perovskites is A_2BX_4, where A is frequently a monovalent organoammonium cation, B is a divalent metal ion, and X is a halide anion. They adopt a layered structure, with corner-sharing $[BX_6]$ octahedra sheets sandwiched between layers of A-site cations, which can result in higher stability in devices compared to their 3D analogs.[2,8,9] The structure of 2D perovskites is highly tunable. For example, the terminal axial halide can be replaced by a linear pseudohalide, SCN^-, resulting in a 2D mixed halide-pseudohalide perovskite. Here, the longer SCN^- effectively separates the inorganic layers such that smaller A site cations (e.g., Cs^+, $CH_3NH_3^+$) can be used. This results in several halide-pseudohalide 2D perovskites featuring shorter interlayer distances compared to the typical all-halide layered perovskites, which have been proposed to result in smaller exciton binding energies.[10−12] Among these pseudohalide 2D perovskites, the all-inorganic materials are particularly interesting due to their enhanced stability.[11−13] The first purely inorganic pseudohalide 2D perovskite single-crystal reported was $Cs_2Pb(SCN)_2Br_2$, which has excellent performance in photodetector applications.[12]

There have been extensive efforts to investigate the dynamical properties of 2D perovskites. Their deformable and highly polar lattices play a central role in the excited-state dynamics by exciton- or charge-lattice interactions.[14,15] It is desirable to understand how the dynamic structural disorder facilitates charge localization, potentially influencing device performance. The structural tunability of 2D perovskites makes them useful for elucidating their complex structural properties, which can aid in tailoring photophysical properties.[16−18] The nitrile stretch in 2D pseudohalide perovskites provides a very useful vibrational probe of lattice dynamics. In addition, the all-inorganic 2D perovskites remove the internal degrees of freedom of organic cations, which leaves only the dynamics of

Received: April 4, 2023
Revised: June 28, 2023

the inorganic octahedral layers. Recently, the dynamic lattice disorder in 2D pseudohalide perovskites was observed by two-dimensional infrared (2D IR) spectroscopy using the nitrile stretch as the vibrational probe. The first experiments were performed on an organic−inorganic perovskite: $(CH_3NH_3)_2Pb(SCN)_2I_2$. The absorption spectrum was shown to be inhomogeneously broadened, and spectral diffusion was determined to occur with a time constant of 4.1 ± 0.3 ps, which is a measure of the rapid interconversion between local structures.[19] We extended the studies of structural dynamics to the purely inorganic perovskites $Cs_2Pb(SCN)_2Br_2$ and $Cs_2Pb(SCN)_2I_2$, which revealed that the spectral diffusion is slower in these perovskites with time constants of 25 and 20 ps, respectively.[20] The $CH_3NH_3^+$ cation has orientational degrees of freedom, which Cs^+ does not have. The loss of these orientational degrees of freedom in the Cs^+ perovskite may result in less dynamic inhomogeneity. This reduction will occur if $CH_3NH_3^+$ assumes different orientations that are not librational motions but rather quasi-stable orientations that exist for a non-negligible length of time, e.g., picoseconds. Upon replacing $CH_3NH_3^+$ with Cs^+, the remaining dynamic disorder observed likely stems from fluctuations in the lead halide-pseudohalide sheets. The local dynamics of 2D octahedra distortions that occur on the timescale of several picoseconds have been suggested to be the origin of the dynamic local disorder of 3D lead halide perovskites.[21] Therefore, tracking the local structural dynamics of 2D octahedra layers is fundamental to a full understanding of the optoelectronic properties of lead halide perovskites regardless of their dimensionality.

Motivated by the previous work, we have expanded the family of all-inorganic X-site substituted 2D perovskites, and characterized the change in dynamic lattice disorder when the structure is modified. We synthesized the first example of an SeCN-containing 2D perovskite $Cs_2Pb(SeCN)_2Br_2$ through a solution-state crystallization method. The selenocyanate-based perovskite permits further investigations of the inorganic cage motion. The considerably longer vibrational lifetime of the CN stretch of selenocyanate provides a substantially increased 2D IR experimental time window, which facilitates a more complete observation of the dynamical lattice disorder. We also performed an investigation of the $SeCN^-$ librations in the $Cs_2Pb(SeCN)_2Br_2$ lattice and compare them to the librations of SCN^- in $Cs_2Pb(SCN)_2Br_2$ via the polarization-selective pump−probe (PSPP) spectroscopy. The vibrational lifetime of the $^{12}C^{14}N$ stretch of the SeCN-perovskite was found to be very long, 213.4 ± 0.8 ps. The long lifetime is discussed in terms of the internal modes of the anions and coupling to lattice phonons.

2. EXPERIMENTAL METHODS

2.1. Synthesis of Isotopically Doped $Pb(SeCN)_2$. Solid $Pb(NO_3)_2$ (40.0 mg) and $KSe^{13}C^{15}N$ (35.1 mg) were separately dissolved in 0.4 mL of water. The $Pb(NO_3)_2$ solution was cooled in an ice bath while stirring, then mixed with the KSeCN solution. The solution was stirred for 10 min, yielding a colorless powder of $Pb(SeCN)_2$ with $Se^{13}C^{15}N$:$Se^{12}C^{15}N$:$Se^{12}C^{14}N$ = 97.4:0.6:2%. The concentration of $Se^{13}C^{14}N$ is too low to be measured. The $KSe^{13}C^{15}N$ as purchased had isotope concentrations of ∼99% ^{13}C and ∼98% ^{15}N. The $Pb(SeCN)_2$ was filtered and dried under reduced pressure overnight. The product was stored in a nitrogen glovebox, avoiding light. The same procedure was used to synthesize isotopically undoped $Pb(SeCN)_2$ using KSeCN.

2.2. Preparation of $Cs_2Pb(SeCN)_2Br_2$ Samples. *2.2.1. Single Crystals.* Solid $Pb(SeCN)_2$ (68.0 mg) and CsBr (20.0 mg) were combined with 170 μL of tetrahydrofuran and 170 μL of dimethyl sulfoxide in a 4 mL scintillation vial in a nitrogen glovebox. The mixture was heated at 60 °C for 10 min. Then, the mixture was filtered through glass microfiber filter paper to yield a light-yellow solution. Dichloromethane was allowed to diffuse into the solution to afford yellow plate-like crystals, among many other side phases.

2.2.2. Powders. Solid CsBr (90.0 mg) and $Pb(SeCN)_2$ (88.2 mg) were loaded into a milling bowl with Zirconia balls (ca. 4 g) in a nitrogen glovebox. The lid was sealed with electrical tape to avoid oxidation from the air. After milling at 800 rpm for 3.5 h, the bowl was transferred into the glovebox and opened. The phase-pure yellow powder product was separated using toluene and dried under reduced pressure overnight.

2.2.3. Thin-Film Preparation. The $Cs_2Pb(SeCN)_2Br_2$ films were spin-coated onto SiO_2-coated (100 nm) CaF_2 substrates in a nitrogen glovebox. Solid CsBr (30.0 mg) and isotopically doped $Pb(SeCN)_2$ (29.4 mg) at a molar ratio of 2:1 were dissolved in 400 μL of a 1:1 *N*,*N*′-dimethylformamide and dimethyl sulfoxide solvent mixture. Mild stirring with heating was applied to fully dissolve the CsBr. The colorless solutions were filtered before spin coating. The precursor solution (100 μL) was loaded onto the substrate, and the substrate was spun at 3000 rpm for 60 s. The as-casted films were then annealed on a hot plate at 80 °C for ∼10 min, resulting in a color change from colorless to yellow. The films were ∼100 nm thick. The phase purity of the films was assessed by powder X-ray diffraction (PXRD) and compared with the simulated pattern (Figure S2).

2.3. Nonlinear Infrared Spectroscopy. *2.3.1. 2D IR Experiments.* The ultrafast IR experiments were conducted with a Ti:Sapphire oscillator/regenerative amplifier producing 800 nm pulses (∼70 fs, 6 W, 3 kHz). Mid-IR pulses are generated by a home-built optical parametric amplifier pumped by the 800 nm pulses. The pulses were centered at 2090 cm^{-1} with a ∼90 cm^{-1} full width at half maximum (FWHM) bandwidth. The 2D IR and PSPP experiments employed a germanium acousto-optic modulator (AOM) pulse shaper.[22] The 2D IR experiments used a pulse sequence of three IR pulses (∼160 fs). The two pump pulses have controlled phases and delay time τ, and the third probe pulse arrives after a waiting time of T_w. The first two pulses and phase cycling to reduce scattered light were generated by the pulse shaper, and a beam split off prior to the pulse shaper by a ZnSe beam splitter produced the third pulse. The T_w delay was set by a mechanical delay line. These three pulses were focused into the sample, and the third pulse stimulated the collinear emission of the vibrational echo pulse. The crossing angle between the pump and probe pulses was 16°. The vibrational echo pulse, which is the signal, was self-heterodyned by the collinear probe pulse, which acted as the local oscillator (LO). The combined signal/LO was steered into a spectrograph and different frequencies were detected with a 32-pixel HgCdTe (MCT) array detector. The 2D IR spectra were obtained by performing two Fourier transforms. The ω_1 axis (horizontal) is given by numerically Fourier-transforming the interferograms that were produced by scanning τ and detected by the array detector at each frequency. The spectrograph takes the time domain echo/LO pulse into the frequency domain, which

https://doi.org/10.1021/acs.jpcc.3c02251
J. Phys. Chem. C XXXX, XXX, XXX−XXX

is an experimental Fourier transform, which gives the ω_3 axis (vertical).

At short T_w, the initial and final frequencies are highly correlated because there has been little time for the structural evolution of the lattice. Therefore, the 2D spectrum along the diagonal exhibits an elongated shape. For later T_ws, the 2D spectrum line shape becomes rounder as the initial frequencies become decorrelated with the final frequencies, resulting from the lattice structural fluctuations. This change in shape is used to determine the normalized frequency−frequency correlation function (FFCF) using the Center Line Slope (CLS) method.[23−25]

The CLS method involves determining the center lines for the 2D spectrum at each T_w. Cuts through the 2D spectrum are made parallel to the vertical axis (ω_3) around the peak of the 2D spectrum. Each cut is a 1D spectrum. The peak frequencies of these 1D spectra are plotted. This plot is the center line. The slopes of the center lines are determined, which are then plotted for each T_w. This plot of the center line slopes corresponds to the normalized FFCF. As discussed below in Section 3.2, there is a small side peak on the red side of the main peak that is studied in the experiments. This side peak distorts the center line on the red side of the 2D spectrum, resulting in a curvature of the center line. Therefore, the center line starting at the peak and going only to the blue side of the 2D spectrum is used to determine the CLS. The small side peak seems to have a vibrational lifetime that is shorter than the main peak, although the peak is too small to measure its lifetime. Its effect on the center line becomes negligible after the first few tens of picoseconds, and the entire line can be used. At these longer times, using the full center line or only the blue side does not change the results. These features, i.e., the side peak and the center lines, can be seen in the figures when they are presented below.

2.3.2. Near-Brewster's Angle Reflection Geometry. The experiments were performed on 2% $^{12}C^{14}N$ to reduce possible excitation transfer and heating effects. Given that the films are very thin and thus have very weak IR absorption, the measurements were conducted in the near-Brewster's angle reflection geometry to enhance the signal-to-noise ratio.[26,27] In this geometry, the probe pulse has an incident angle of 53° on the sample, which is close to Brewster's angle. The near-Brewster's angle reflection amplitude of the probe pulse (pulse 3 in the sequence) is greatly diminished, while the signal field, which is emitted in the same reflection direction for very thin films, is virtually unchanged. The desired information is the modulation of the intensity of the probe pulse by the heterodyned (Signal × LO). Reducing probe reflection intensity reduces $|LO|^2$. However, the signal × LO is reduced linearly, so the percent modulation was enhanced by ∼30 in the reflection geometry, which is essential for acquiring high-quality 2D IR data from the thin films.

2.3.3. PSPP Spectroscopy. In the PSPP experiments, the mechanical delay stage is utilized to scan the temporal separation, t, between the single pump pulse and probe pulse. From the time-dependent pump−probe signal, we can obtain population relaxation and anisotropy. A half-wave plate and polarizer are used to set the pump polarization to 45°, and the probe pulse is set to be s-polarized (90°, vertical polarization). After the sample, a computer-controlled polarizer is alternated between parallel (+45°) and perpendicular (−45°) relative to the pump polarization to resolve signals with polarizations parallel ($I_{\parallel}(t)$) and perpendicular ($I_{\perp}(t)$) relative to the pump pulse. The PSPP experiments were conducted in the small incidence angle reflection geometry, which preserves the relative polarizations of the pulse when they enter the sample.[20] In this near-normal reflection geometry, the signal is enhanced ∼5 compared to the usual transmission detection.

3. RESULTS AND DISCUSSION

3.1. Structure of $Cs_2Pb(SeCN)_2Br_2$. The single-crystal X-ray diffraction (SC-XRD) structure for $Cs_2Pb(SeCN)_2Br_2$ was solved in the *Pmmn* space group at 100 K and room temperature (see Supporting Information for the crystallographic data summary). As illustrated in Figure 1, this material

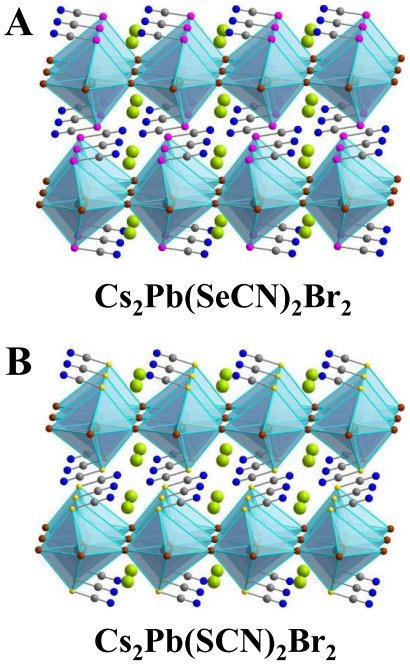

Figure 1. (A) Crystal structure of the $Cs_2Pb(SeCN)_2Br_2$ perovskite. (B) Crystal structure of the $Cs_2Pb(SCN)_2Br_2$ perovskite. Green, turquoise, brown, yellow, pink, gray, and blue spheres correspond to Cs, Pb, Br, S, Se, C, and N atoms, respectively.

closely resembles the SCN-analog $Cs_2Pb(SCN)_2Br_2$ in structure, with corning-sharing $[PbX_2Br_4]^{4-}$ (X = $SeCN^-$, SCN^-) octahedra forming layers. (A figure with the two structures overlaid is given in the SI, Figure S3.) The $SeCN^-$ ions occupy the axial positions in the octahedral unit and are perfectly antiparallel to each other between the layers. The room-temperature unit-cell volume increases by 2.87% compared to that of $Cs_2Pb(SCN)_2Br_2$. The b and c axes (along the inorganic sheets) of $Cs_2Pb(SeCN)_2Br_2$ increase by 0.84 and 1.3%, respectively, compared to those in $Cs_2Pb(SCN)_2Br_2$, whereas the a axis (perpendicular to the inorganic sheets) only expands by 0.48%. These somewhat counterintuitive lattice changes can be explained by the orientation of the pseudohalides in the structure (bond angles: Pb−Se−C: 91.3°; Pb−S−C: 96.4°) and the larger size of $SeCN^-$ (Pb−Se bond length: 3.07 Å; Pb−S bond length: 2.94 Å). In the rest of this paper, $Cs_2Pb(SCN)_2Br_2$ and $Cs_2Pb(SeCN)_2Br_2$ will be referred to as the SCN- and SeCN-perovskite, respectively.

3.2. Absorption Spectra. The linear absorption spectrum of the CN stretch of the SeCN-perovskite is presented in Figure 2. Since the isotope we utilized was $Se^{13}C^{15}N^-$, peaks

https://doi.org/10.1021/acs.jpcc.3c02251
J. Phys. Chem. C XXXX, XXX, XXX−XXX

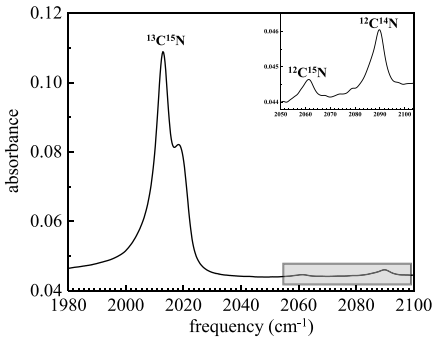

Figure 2. FT-IR absorption spectra of the CN stretching region of the $Cs_2Pb(SeCN)_2Br_2$ film. Inset: expanded view of $^{12}C^{15}N$ and $^{12}C^{14}N$ modes. Both modes have asymmetric shapes.

corresponding to the $^{13}C^{15}N$, $^{12}C^{15}N$, and $^{12}C^{14}N$ can be observed in the spectrum. Because of the negligible concentration of $^{13}C^{14}N$ species, the intensity of its peak is too low to observe.

The most intense absorption is assigned to the $^{13}C^{15}N$ stretch, which is split into two bands at 2013 and 2019 cm^{-1}. The vibrational splitting of high-concentration species has been observed in all of the pseudohalide perovskites we studied before.[19,20] It was initially ascribed to the transition dipole-transition dipole coupling between the two adjacent CN stretches in different layers that are close together.[19] The coupling of this CN pair should lead to two vibrational eigenstates that are the sum and difference of the CN stretches of the two anions. The transition dipoles of the two eigenstates are the sum and difference of the individual transition dipoles, one for the anion in each layer. Because the two anions are antiparallel, the transition dipole of one of the eigenstates is identically zero. Therefore, the coupling between the anions in adjacent layers will not result in two peaks in the spectrum. Instead, it was later proposed that the splitting arises from the two anions that are coordinated to the same Pb^{2+}. These anions are not parallel. The interaction of the $SeCN^-$ and the Pb^{2+} should have a substantial covalent character. Therefore, the CN stretches of the two anions bound to the Pb^{2+} can be coupled by through-bond interactions. The result is two normal modes, i.e., the sum and difference of the two CN local modes. Because the local mode transition dipoles are not parallel, both normal modes will have non-zero transition dipoles.

The $^{12}C^{14}N$ peak is centered at 2090 cm^{-1}, and it is asymmetric with a shoulder on the lower frequency side. The concentration of $^{12}C^{14}N$ species is sufficiently low not to result in peak splitting. Most of the $SeCN^-$s are $^{13}C^{15}N$. Only 1−2% are $^{12}C^{14}N$, which gives rise to the band at 2090 cm^{-1}, on which we do the experiments. Therefore, the vast majority of the$^{12}C^{14}N$s we study will have $^{13}C^{15}N$ as the other $SeCN^-$ bound to a Pb^{2+}. The separation between the $^{12}C^{14}N$ and $^{13}C^{15}N$ peaks is ∼74 cm^{-1}. The coupling is ∼2.5 cm^{-1} (half of the splitting of the $^{13}C^{15}N$ band). The coupling is small compared to the $^{12}C^{14}N$ and $^{13}C^{15}N$ peaks' separation. Therefore, the $^{12}C^{14}N$ peak studied in the experiments is composed of CN stretch local modes, and the peak will not be split through interaction with the other $SeCN^-$ bound to a Pb^{2+}.

The $^{12}C^{14}N$ peak centered at 2090 cm^{-1} is asymmetric and cannot be fit with a single Voigt function. While it is not as evident in the spectrum of the SeCN-perovskite, it was found for the SCN-perovskite, that the low frequency shoulder is caused by a small side peak.[20] The side peak is shifted from the main peak by ∼5 cm^{-1} with a slightly larger FWHM. Temperature dependent FT-IR spectra on the SCN-perovskite explicated the nature of the side peak and provided information on its nature.[20] At low temperature (120 K), the side peak was too small to detect. As the temperature was increased, the side peak grew in. The temperature dependent amplitude of the side peak was plotted as the log of the absorbance versus the inverse of temperature. The data points fit to a straight line, indicating an activated process with an activation energy of ∼160 cm^{-1}. A reasonable explanation for the SCN^- side peak is that there are sites with two distinct conformations in the lattice resulting from two potential wells. The main peak arises from SCN^-s that occupy the lower energy well, and the side peak arises from SCN^-s that occupy the higher energy well. Because of the similarities of the room temperature spectra, we assume that the SeCN-perovskite side peak arises for the same reason.

The small feature at 2061 cm^{-1} arises from the $^{12}C^{15}N$ stretch, and it also has an asymmetric shape. The similarity between the $^{12}C^{14}N$ and $^{12}C^{15}N$ peak shapes further indicates that the shoulder is caused by a side peak as in their SCN-analogs. The peak of the $^{12}C^{15}N$ stretch has an FWHM of ∼5 cm^{-1} like the $^{12}C^{14}N$ stretch.

3.3. Lifetime Measurement. As discussed above, there are three bands in the spectrum associated with the different isotopes. When measuring the PSPP signal reported by a certain isotope mode, two spectral holes were created in the frequency domain by the AOM pulse shaper with a Hann window to avoid exciting the other two isotope bands. The data before 7 ps were removed to avoid time domain artifacts created by spectral filtering in the early times. The same procedures were used for the 2D IR measurements presented in the following section. Because the dynamics are relatively slow, eliminating the first 7 ps does not interfere with the data analysis.

The population decay, $P(t)$ (lifetime) was obtained using the equation[28,29]

$$P(t) = [I_{\parallel}(t) + 2I_{\perp}(t)]/3 \quad (1)$$

Figure 3 displays the lifetime decay of the $^{12}C^{14}N$ stretch of the SeCN-perovskite. The lifetime is 213.4 ± 0.8 ps, which is much longer than that of the SCN-perovskites (∼56 ps). The vibrational lifetime of a probe is very sensitive to its chemical composition. A heavy atom can separate the CN stretch from

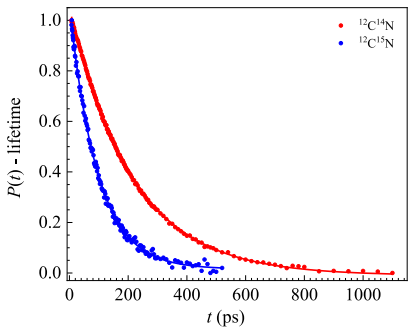

Figure 3. Vibrational population decays of $^{12}C^{14}N$ (red) and $^{12}C^{15}N$ (blue) stretching modes. The lifetimes are determined to be 213.4 ± 0.8 and 95.6 ± 0.8 ps for the $^{12}C^{14}N$ and $^{12}C^{15}N$ modes, respectively.

https://doi.org/10.1021/acs.jpcc.3c02251
J. Phys. Chem. C XXXX, XXX, XXX−XXX

coupling to intramolecular modes that can serve as vibrational population relaxation pathways. Due to its heavier mass, the selenium atom more effectively suppresses intramolecular relaxation of the CN stretch to the energy-accepting modes than the sulfur atom. In addition, we measured the lifetime reported by the $^{12}C^{15}N$ stretch and the decay is also a single exponential with a lifetime of 95.6 ± 0.8 ps, significantly shorter than the $^{12}C^{14}N$ stretch. The isotopic effect on vibrational lifetime has been observed in many systems,[20,30,31] and it is attributed to the change in intramolecular vibrational relaxation by the isotope substitution.

Coupling of the CN stretch with other intramolecular vibrations and lattice phonons gives rise to vibrational relaxation.[32] There are many possible relaxation pathways. Here we will consider several possibilities to provide insight into the relaxation process. Generally, the lower the order of the relaxation pathway (fewer modes involved) is, the faster the relaxation will be.[32] $SeCN^-$ has three normal modes; other than one CN stretch, there is one Se−C stretch and two degenerate SeCN bends. Their vibrational frequencies are 560 and 420 cm^{-1}, respectively.[33,34] Consider the following possible relaxation pathways. The initial $^{12}C^{14}N$ stretch (2090 cm^{-1}) is annihilated, five quanta of the 420 cm^{-1} bend are created (2100 cm^{-1}), and a 10 cm^{-1} phonon is annihilated (in this qualitative discussion the unknown anharmonicities are not considered). This is a 7th order process that conserves energy. However, there are two 6th order processes. The CN stretch is annihilated, 4 quanta of the bend are created (2240 cm^{-1}), and a 150 cm^{-1} phonon is annihilated. While the phonon dispersion is not known for the SeCN-perovskite under study here or the previously investigated SCN-perovskite, typical maximum phonon energies for a variety of lead halide perovskites are in the range of ∼30 to ∼60 cm^{-1}.[35,36] So, the requirement of a 150 cm^{-1} phonon would not make the 6th order process possible. Another candidate is that the CN stretch is annihilated, three quanta of the stretch and one quanta of bend are created (2100 cm^{-1}), and a 10 cm^{-1} phonon is annihilated. This 6th order mechanism is possible, which can give rise to the long vibrational lifetime. For $Se^{12}C^{15}N^-$, the CN stretch band is at 2061 cm^{-1}. The $Se^{12}C^{15}N^-$ bend and stretch frequencies will be almost the same as those of $Se^{12}C^{14}N^-$. Everything will be the same except a 38 cm^{-1} phonon will be annihilated. The higher frequency phonon may have a larger density of states, and its shorter wavelength should couple better to the CN stretch. These considerations may be responsible for the factor of ∼2 shorter lifetime for the $^{12}C^{15}N$ stretch.

3.4. Anisotropy. In isotropic three-dimensional systems, the anisotropy is proportional to the second Legendre polynomial orientational correlation function by[28,29]

$$r(t) = \frac{I_{\parallel}(t) - I_{\perp}(t)}{I_{\parallel}(t) + 2I_{\perp}(t)} = 0.4C_2(t) \quad (2)$$

A probe molecule in a liquid will undergo complete diffusive orientational relaxation, which will cause the anisotropy to decay to zero. However, in the small crystals that make up the SeCN-perovskite thin films, the anions occupy fixed lattice sites. They will not undergo diffusive orientational relaxation. However, very fast librational motions will cause the $SeCN^-$ to sample a cone of angles. This sampling is too fast (<100 fs) for our instrument to measure. The limited range of sampling causes the anisotropy to be less than 0.4 when the measured anisotropy curve is extrapolated to $t = 0$. Using this value, the cone of angles that have been sampled can be determined. Then from the cone of angles, the harmonic cone model can be used to determine the librational potential energy.

In determining the lifetime (eq 1), the sum of signals, $I_{\parallel}(t) + 2I_{\perp}(t)$ is used. For the anisotropy, it is necessary to take the difference, $I_{\parallel}(t) - I_{\perp}(t)$. Taking the difference of weak signals results in a degraded signal-to-noise ratio. To obtain reasonable data, we increased the concentration to ∼2% $^{12}C^{14}N$. This results in a small amount of vibrational excitation transfer between CNs with transition dipoles pointing in different directions. The excitation transfer causes the anisotropy to have a slight decay (see Figure 4). However, we extrapolated the decay to $t = 0$ to obtain information about the inertial motions.

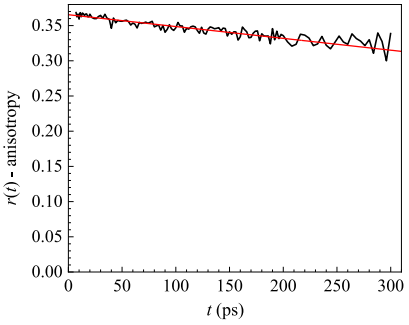

Figure 4. Anisotropy decay reported by the $^{12}C^{14}N$ stretch. The slight decay possibly arises from the excitation transfer between different orientations of $^{12}C^{14}N$. Of interest here is the difference between the intercept at $t = 0$ (see red line) and the maximum value of 0.4. This difference is related to the range of angles sampled by libration of the $SeCN^-$ (see text).

Because the CN dipoles are not randomly distributed in the perovskite lattice, the three-dimensional anisotropy model is insufficient to describe the orientational dynamics of $SeCN^-$s. The transition dipoles (CN bond axis) wobble in cones that are tilted out of the planes of the plate-like crystals that lie with the inorganic sheets parallel to the spin-coated substrate. The method of addressing this issue has been developed in previous publications,[20,37,38] and applied to the SCN-perovskite.[20] The observed parallel and perpendicular signals for the ensemble of tilted cones are

$$I_{\parallel} = \left[1 - 2\langle S\rangle + C_{op}(t) + \frac{9}{8}C_{mip}(t)\right] \times P(t)$$
$$I_{\perp} = \left[1 - 2\langle S\rangle + C_{op}(t) - \frac{9}{8}C_{mip}(t)\right] \times P(t) \quad (3)$$

where $\langle S\rangle$ is the order parameter, $C_{op}(t)$ and $C_{mip}(t)$ are the out-of-plane and mainly in-plane components of the orientational correlation functions, respectively.

We first utilized the well-known wobbling-in-a-cone model[39−41] to analyze the inertial motions of $SeCN^-$s. Because their distribution is non-isotropic in space, the wobbling-in-a-cone theory has to be adapted for the uniaxial systems.[37,38] In this case, given that only the ultrafast librational motions contribute to the initial anisotropy drop, $\langle S\rangle$, $C_{op}(t)$, and $C_{mip}(t)$ can be evaluated in the infinite time limit to obtain the cone angle. In the infinite time limit the equations simplify to[20]

https://doi.org/10.1021/acs.jpcc.3c02251
J. Phys. Chem. C XXXX, XXX, XXX−XXX

$$\langle S \rangle = \frac{3\cos^2\theta_t - 1}{4}\cos\theta_c(1 + \cos\theta_c) \quad (4)$$

$$C_{op}(t) = \frac{(3\cos^2\theta_t - 1)^2}{16}[\cos\theta_c(1 + \cos\theta_c)]^2 \quad (5)$$

$$C_{mip}(t) = \frac{\sin^4\theta_t}{4}[\cos\theta_c(1 + \cos\theta_c)]^2 \quad (6)$$

where θ_t is the cone tilt angle and θ_C is the cone half angle. θ_t is the tilt angle from the normal to the plane, which was determined to be 79° from the single-crystal X-ray structure. $r(t)$ is derived from combining the equations. Then θ_C can be numerically obtained from $r(t)$, which was determined to be $\theta_C = 14 \pm 2°$ for the SeCN-perovskite. The half-cone angle is the same within experimental error as the reported value for the SCN-perovskite.[20] The two crystal structures are very similar, and the cone of angles sampled by the pseudohalides are the same within error.

It is possible to obtain useful information about the librational potential from the cone angle using the harmonic cone theory.[42,43] The standard wobbling-in-a-cone theory provides information on the cone angles and dynamics from the experimental anisotropy measurements of motion in a cone with hard walls. The librational motions of the pseudohalides in a crystal are not diffusive and the motions are not controlled by collisions with surrounding molecules in a liquid. Rather, these anions are in a crystal lattice, and the extent of their librational motions at a given temperature is determined by the angular potential. In the harmonic cone theory, the librational potential is modeled as a 2D parabola.[42] Taking the librational dynamics to occur on a 2D harmonic potential energy surface, we can obtain the characteristic harmonic oscillator frequency for the surface. For cone half angles less than 30°, there is a simple relation between the hard cone half angle and the harmonic cone angle.[43] For angles greater than 30°, there is a full relation, which requires numerical integration.[42,43] Here, we are in the small angle limit. The oscillator frequency is obtained from the harmonic cone's half-angle from[43,44]

$$\omega^2 = \frac{kT}{I\theta_H^2} \quad (7)$$

where I is the moment of inertia calculated from the bond lengths obtained from the single-crystal structure ($I_{SCN^-} = 1.36 \times 10^{-45}$, $I_{SeCN^-} = 2.06 \times 10^{-45}$ kg m^2), k is Boltzmann's constant, and T is the absolute temperature. θ_H is the harmonic cone half angle that contains 95% of librational angular excursions. It has been shown that the half-cone angle extracted from the hard cone model (θ_C) is related to the half angle from the harmonic cone model by $2\theta_H = \theta_C$, in the small angle limit.[43] The oscillator frequencies were determined to be 81 and 61 cm^{-1} for the SCN- and SeCN-perovskites, respectively. The extents of angular sampling are basically the same in the two crystals. kT at room temperature is ~200 cm^{-1}. Therefore, there is a significant thermal excitation of the pseudohalides in both crystals. The SCN^- libration has an occupation number of ~2, while $SeCN^-$ has an occupation number of ~2.8. Therefore, thermal excitation contributes to the range of angles sampled.

The frequencies and thermal populations of the librations may play a role in the dynamics of electronic excited states, i.e., excitons and charge carriers. As mentioned above, the phonon dispersions are not known for the SeCN or SCN-perovskites, but the typical maximum phonon energies of lead halide perovskites (Debye cutoff), in general, range from ~30 to ~60 cm^{-1}.[35,36] These are very low energies. In the 2D purely inorganic pseudohalide perovskites, there are no small organic cations that have intramolecular and intermolecular high frequency modes. Depending on the energy of the Debye cutoff, excitation of the librations could require two or more phonons. The room temperature excited librations may be able to transfer energy to an electronic excited state. These modes could play a role by scattering excitons and charge carriers.

3.5. Spectral Diffusion. As shown by the data presented below, the CN stretch absorption spectrum is inhomogeneously broadened. Inhomogeneous broadening is caused by a distribution of environments of the $SeCN^-$ that have distinct couplings to the CN, which shift its frequency. A portion of the inhomogeneous broadening is dynamic, which is caused by the structural dynamics of the lattice. Therefore, the CN frequencies evolve over time. The time-dependent sampling of a range of frequencies is referred to as spectral diffusion.

When the structure of the lattice in the vicinity of an SCN^- changes, the interactions with the anion will change. The CN stretch has substantial Stark coupling that contributes to the inhomogeneous linewidth.[45] Small changes in the lattice configuration can produce changes in the electric field along the CN bond vector. Such changes will cause the vibrational frequency to change, giving rise to spectral diffusion, that is, sampling of different frequencies within the absorption spectrum. Contributions of the inhomogeneous and homogeneous absorption line broadening can be distinguished by 2D IR spectroscopy. The homogeneous contribution to the absorption line is caused by the coupling of the SCN^- to phonons[46−48] as opposed to relatively long-lived lattice distortions that give rise to inhomogeneous broadening. The phonons may be acoustic or optical including librations. The phonon lattice motions must modulate the CN stretch frequency to cause homogeneous dephasing.[46−48]

Figure 5 displays the 2D IR spectra acquired at $T_w = 7$ and 300 ps. The long vibrational lifetime of $SeCN^-$ enables us to extend our observation window to a much longer time compared to the SCN-perovskite. The information on the dynamics is contained in the change in the shape of the 2D spectrum with increasing T_w. The center lines are shown as the white dots in the plots.[23−25] The change in the central line slope with T_w, CLS(T_w), is the normalized FFCF.

Figure 6 shows the CLS(T_w) decay obtained by averaging the data from several separately prepared samples. The CLS(T_w) is the normalized FFCF. The time constants are correct, but the amplitudes are relative, they are a fraction of 1 for a particular component. The decay of the CLS(T_w) demonstrates the existence of dynamic inhomogeneity. The decay is a single exponential with a time constant of 48 ± 4 ps. The time constant for the SCN-perovskite is 24.6 ± 3.3 ps. Therefore, the spectral diffusion, reflecting structural fluctuations originating from dynamic lattice disorder, is a factor of ~2 slower in the SeCN-perovskite.

The CLS(T_w) decays to a constant value rather than zero. There are two possible reasons for a decay to a non-zero value. The first is that there may be one or more components of spectral diffusion that are much slower than the experimental time window. Then over the observation period, the slow component does not decay, appearing constant in the experiment. The other possibility is that there is static inhomogeneity in the sample that will not randomize on any

https://doi.org/10.1021/acs.jpcc.3c02251
J. Phys. Chem. C XXXX, XXX, XXX−XXX

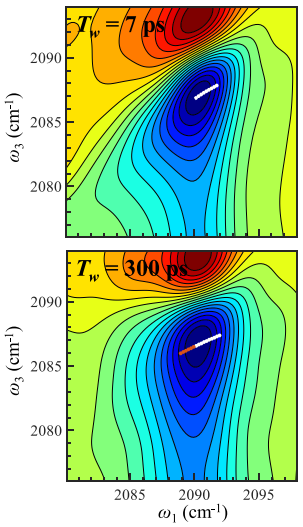

Figure 5. 2D IR spectra of the $^{12}C^{14}N$ stretch at T_w = 7 (top) and 300 ps (bottom) acquired by the spectrally filtered pump pulse that only pumps the $^{12}C^{14}N$ stretch. The center lines, which are used to quantitatively analyze the spectral diffusion dynamics using the CLS method, are shown as the white dots. The orange dots along with the white dots in the bottom figure show that at later T_ws, the center line has become essentially straight. Only the blue side of the main absorption peak was analyzed for extracting the CLS decay.

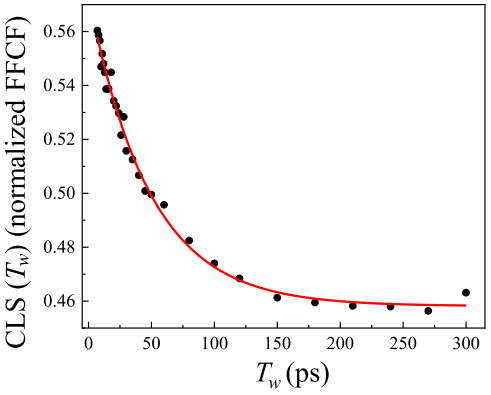

Figure 6. CLS(T_w) (normalized frequency−frequency correlation function) decay obtained from the average of data taken on several separately prepared samples. The data were fitted with a single exponential with an offset, and the decay time constant is determined to be 48 ± 4 ps. The offset is caused by static or very slowly evolving lattice inhomogeneity.

time scale. The sample is a thin film of microcrystals. The crystallites that comprise the films can have strains and defects that will give rise to static inhomogeneity. There is some evidence for static inhomogeneity. Different samples essentially gave the same decay constants within experimental error. However, the long-time offset varies somewhat from sample to sample. The variation is far outside of experimental error (see Figure S6). This behavior could occur if the preparation of the spin-coated samples resulted in crystallites with different amounts of strain and defects from one sample to another, possibly due to small differences in grain size or thickness. Variations in grain size and thickness, which could lead to different degrees of static inhomogeneous broadening, possibly stem from variations of the substrate surface, the concentration of the precursor solution, the annealing time, and the atmosphere inside the glovebox.

We can separate the homogeneous and inhomogeneous dynamics by analyzing the CLS decay curve. The ratio of the initial CLS value and 1 is a measure of homogeneous broadening. The experimental initial CLS value is obtained via extrapolation of the decay curve to T_w = 0 ps, which gives 0.57 ± 0.02. Using the CLS(T_w) and the FWHM of the main absorption peak, the full FFCF was obtained.[25] The homogeneous and inhomogeneous widths are 2.5 and 3.4 cm^{-1}, respectively. The inhomogeneous width has two components; the dynamic width that is associated with spectral diffusion, Δ_D, and the static width, Δ_S, which comes from the offset of the decay in Figure 6. The total inhomogeneous width is $(\Delta_D^2 + \Delta_s^2)^{1/2}$. Then Δ_D = 1.3 and Δ_S = 3.1 cm^{-1}. The total width, with homogeneous and inhomogeneous contributions, is ∼5 cm^{-1}.

Both the homogeneous and the dynamic inhomogeneous disorder are different from those found for the SCN-perovskite. In the SCN-perovskite, the homogeneous broadening is 2.8 cm^{-1} compared to a total linewidth of 4 cm^{-1}, giving a ratio of 0.7.[20] In contrast, the homogeneous broadening of the SeCN-perovskite is 2.5 cm^{-1} compared to a total linewidth of 5 cm^{-1}, giving a ratio of 0.5. As discussed above, the homogenous linewidth is caused by coupling of the CN to lattice phonons.[46−48] Therefore, in the SCN-perovskite, the CN coupling to phonons is greater. The phonons are thermally excited motions of the lattice. The homogeneous broadening is a result of phonon induced frequency fluctuations of the CN stretch. Because the CN moiety is the same in the two perovskites, either the extent of the lattice fluctuations is greater and/or the coupling to phonon modes is larger in the SCN-perovskite. One possibility is that the coupling is greater in the SCN-perovskite because the Pb−S bond is stronger than the Pb−Se bond (larger bond enthalpy). The Pb−Se and Pb−S bond association energies are reported as 303 and 346 kJ/mol,[49,50] respectively, although these values may differ to some extent in the perovskite systems. Then phonons that modulate these bonds may have a larger effect on the electron density of the S than the Se, resulting in larger phonon coupling to the CN frequency.

The dynamic inhomogeneous broadening of the CN in the SeCN-perovskite is greater than it is in the SCN-perovskite (Δ_D = 0.9 and Δ_S = 1.9 cm^{-1})[20] by ∼50%. The dynamic inhomogeneous broadening is caused by dynamic lattice interconversions between different local minima (structural configurations) of the energy landscape. Dynamic inhomogeneity is distinct from phonon dynamics that would still exist in a perfect lattice. Compared to the SCN^- counterpart, the spectral diffusion (inhomogeneous structural dynamics) in the SeCN-perovskite is somewhat more extensive and approximately a factor of 2 slower.

4. CONCLUDING REMARKS

This paper presents the synthesis of the 2D pseudohalide perovskite $Cs_2Pb(SeCN)_2Br_2$ as single crystals, powders, and thin films. The CN stretch of the pseudohalide, $SeCN^-$, is an excellent IR probe for conducting 2D IR and PSPP experiments on $Cs_2Pb(SeCN)_2Br_2$ thin films. The $Cs_2Pb(SeCN)_2Br_2$ thin films were prepared with ∼98% $Se^{13}C^{15}N^-$ and the experiments were conducted on $Se^{12}C^{14}N^-$ to avoid vibrational excitation transfer. The $^{12}C^{14}N$ has a very long vibrational lifetime of over 200 ps, which allows us to examine

https://doi.org/10.1021/acs.jpcc.3c02251
J. Phys. Chem. C XXXX, XXX, XXX−XXX

the spectral diffusion dynamics over an unprecedented timescale. The long lifetime brings clarity to some features observed in previous experiments on 2D pseudohalide perovskites.[19,20] From the measured anisotropy decay, we determined the half-cone angle of the librational motions of the $SeCN^-$ in the $Cs_2Pb(SeCN)_2Br_2$ crystal lattice. The harmonic cone model,[42−44] was used to analyze the measured cone half-angle of $Cs_2Pb(SeCN)_2Br_2$ and the cone half-angle previously reported for $Cs_2Pb(SCN)_2Br_2$. The harmonic cone model gives the harmonic oscillator frequency of the 2D librational potential energy surface. The SCN- and SeCN-perovskites have somewhat different pseudohalide oscillator frequencies.

High-quality 2D IR spectra were acquired, and the data reveal that the $Cs_2Pb(SeCN)_2Br_2$ lattice exhibits dynamic disorder on a ∼50 ps timescale. This study demonstrates the impact of changing the pseudohalide anions on the lattice structural evolution in 2D pseudohalide perovskites. The inhomogeneous structural dynamics differ in the SeCN- and SCN-perovskites. The structural evolution is ∼2 times slower in the SeCN-perovskite, and there is a greater range of CN frequencies sampled. The long CN stretch lifetime in the SeCN-perovskite made it possible to unambiguously observe that the data go to a non-zero value offset at long time. The offset is most likely caused by static inhomogeneity of the lattice.

These results can have important implications when considering charge-lattice interactions in perovskites. Excitons and charge carriers experience both phonon dynamics and dynamic lattice inhomogeneity. The dynamic inhomogeneous disorder can both trap excited carriers and promote excited carriers out of lattice traps.

To date, all of the IR nonlinear experiments have been conducted on 2D layered pseudohalide perovskites with Pb^{2+} cations. It will be informative to extend the studies of lattice dynamics by expanding the family of 2D pseudohalide perovskites to those with different B-site cations. In addition, these experiments suggest the possibility of using ultrafast nonlinear IR experiments to directly probe the nature of inhomogeneous lattice dynamics on the photo-excited states of perovskites.

■ ASSOCIATED CONTENT

Supporting Information

The Supporting Information is available free of charge at https://pubs.acs.org/doi/10.1021/acs.jpcc.3c02251.

Crystal structure determination; powder X-ray diffraction; absorption measurements; supplementary figures and tables (PDF)

■ AUTHOR INFORMATION

Corresponding Authors

Hemamala I. Karunadasa − *Department of Chemistry, Stanford University, Stanford, California 94305, United States; Stanford Institute for Materials and Energy Sciences, SLAC National Accelerator Laboratory, Menlo Park, California 94025, United States;* orcid.org/0000-0003-4949-8068; Phone: 650 723-0288; Email: hemamala@stanford.edu

Michael D. Fayer − *Department of Chemistry, Stanford University, Stanford, California 94305, United States;* orcid.org/0000-0002-0021-1815; Phone: 650 723-4446; Email: fayer@stanford.edu

Authors

Xiangyu Xing − *Department of Chemistry, Stanford University, Stanford, California 94305, United States*

Jiayi Li − *Department of Chemistry, Stanford University, Stanford, California 94305, United States*

John P. Breen − *Department of Chemistry, Stanford University, Stanford, California 94305, United States*

Complete contact information is available at: https://pubs.acs.org/10.1021/acs.jpcc.3c02251

Author Contributions

X.X. and J.L. contributed equally. The manuscript was written through contributions of all authors.

Notes

The authors declare no competing financial interest.

■ ACKNOWLEDGMENTS

This work was supported by the Air Force Office of Scientific Research grant number FA9550-16-1-0104 (X.X., J.P.B., and M.D.F.). Work by J.L. and H.I.K. was funded by the National Science Foundation (DMR-1904443). J.L. is grateful for a Stanford Interdisciplinary Graduate Fellowship. Part of this work was performed at the Stanford Nano Shared Facilities (SNSF), supported by the National Science Foundation under Award No. ECCS-2026822.

■ REFERENCES

(1) Ishihara, T.; Takahashi, J.; Goto, T. Exciton State in Two-Dimensional Perovskite Semiconductor $(C_{10}H_{21}NH_3)_2PbI_4$. *Solid State Commun.* **1989**, *69*, 933−936.

(2) Smith, I. C.; Hoke, E. T.; Solis-Ibarra, D.; McGehee, M. D.; Karunadasa, H. I. A Layered Hybrid Perovskite Solar-Cell Absorber with Enhanced Moisture Stability. *Angew. Chem., Int. Ed.* **2014**, *53*, 11232−11235.

(3) Tsai, H.; Nie, W.; Blancon, J.-C.; Stoumpos, C. C.; Asadpour, R.; Harutyunyan, B.; Neukirch, A. J.; Verduzco, R.; Crochet, J. J.; Tretiak, S.; et al. High-Efficiency Two-Dimensional Ruddlesden−Popper Perovskite Solar Cells. *Nature* **2016**, *536*, 312−316.

(4) Li, L.; Sun, Z.; Wang, P.; Hu, W.; Wang, S.; Ji, C.; Hong, M.; Luo, J. Tailored Engineering of an Unusual $(C_4H_9NH_3)_2(CH_3NH_3)_2Pb_3Br_{10}$ Two-Dimensional Multilayered Perovskite Ferroelectric for a High-Performance Photodetector. *Angew. Chem., Int. Ed.* **2017**, *56*, 12150−12154.

(5) Yuan, M.; Quan, L. N.; Comin, R.; Walters, G.; Sabatini, R.; Voznyy, O.; Hoogland, S.; Zhao, Y.; Beauregard, E. M.; Kanjanaboos, P.; et al. Perovskite Energy Funnels for Efficient Light-Emitting Diodes. *Nat. Nanotechnol.* **2016**, *11*, 872−877.

(6) Gong, X.; Voznyy, O.; Jain, A.; Liu, W.; Sabatini, R.; Piontkowski, Z.; Walters, G.; Bappi, G.; Nokhrin, S.; Bushuyev, O.; et al. Electron−Phonon Interaction in Efficient Perovskite Blue Emitters. *Nat. Mater.* **2018**, *17*, 550−556.

(7) Qin, C.; Sandanayaka, A. S. D.; Zhao, C.; Matsushima, T.; Zhang, D.; Fujihara, T.; Adachi, C. Stable Room-Temperature Continuous-Wave Lasing in Quasi-2D Perovskite Films. *Nature* **2020**, *585*, 53−57.

(8) Slavney, A. H.; Smaha, R. W.; Smith, I. C.; Jaffe, A.; Umeyama, D.; Karunadasa, H. I. Chemical Approaches to Addressing the Instability and Toxicity of Lead−Halide Perovskite Absorbers. *Inorg. Chem.* **2017**, *56*, 46−55.

(9) Zhao, X.; Liu, T.; Loo, Y.-L. Advancing 2D Perovskites for Efficient and Stable Solar Cells: Challenges and Opportunities. *Adv. Mater.* **2022**, *34*, No. 2105849.

(10) Daub, M.; Hillebrecht, H. Synthesis, Single-Crystal Structure and Characterization of $(CH_3NH_3)_2Pb(SCN)_2I_2$. *Angew. Chem., Int. Ed.* **2015**, *54*, 11016−11017.
(11) Li, C.-H.; Tsai, C.-C.; Liao, M.-Y.; Su, Y.-A.; Lin, S.-T.; Chueh, C.-C. Stable, Color-Tunable 2D SCN-Based Perovskites: Revealing the Critical Influence of an Asymmetric Pseudo-Halide on Constituent Ions. *Nanoscale* **2019**, *11*, 2608−2616.
(12) Liao, C.-H.; Chen, C.-H.; Bing, J.; Bailey, C.; Lin, Y.-T.; Pandit, T. M.; Granados, L.; Zheng, J.; Tang, S.; Lin, B.-H.; et al. Inorganic-Cation Pseudohalide 2D $Cs_2Pb(SCN)_2Br_2$ Perovskite Single Crystal. *Adv. Mater.* **2022**, *34*, No. 2104782.
(13) Numata, Y.; Sanehira, Y.; Ishikawa, R.; Shirai, H.; Miyasaka, T. Thiocyanate Containing Two-Dimensional Cesium Lead Iodide Perovskite, $Cs_2PbI_2(SCN)_2$: Characterization, Photovoltaic Application, and Degradation Mechanism. *ACS Appl. Mater. Interfaces* **2018**, *10*, 42363−42371.
(14) Zhu, H.; Miyata, K.; Fu, Y.; Wang, J.; Joshi, P. P.; Niesner, D.; Williams, K. W.; Jin, S.; Zhu, X.-Y. Screening in Crystalline Liquids Protects Energetic Carriers in Hybrid Perovskites. *Science* **2016**, *353*, 1409−1413.
(15) Miyata, K.; Meggiolaro, D.; Trinh, M. T.; Joshi, P. P.; Mosconi, E.; Jones, S. C.; De Angelis, F.; Zhu, X.-Y. Large Polarons in Lead Halide Perovskites. *Sci. Adv.* **2017**, *3*, No. e1701217.
(16) Quan, L. N.; Park, Y.; Guo, P.; Gao, M.; Jin, J.; Huang, J.; Copper, J. K.; Schwartzberg, A.; Schaller, R.; Limmer, D. T.; et al. Vibrational Relaxation Dynamics in Layered Perovskite Quantum Wells. *Proc. Natl. Acad. Sci. U. S. A.* **2021**, *118*, No. e2104425118.
(17) Koegel, A. A.; Mozur, E. M.; Oswald, I. W. H.; Jalarvo, N. H.; Prisk, T. R.; Tyagi, M.; Neilson, J. R. Correlating Broadband Photoluminescence with Structural Dynamics in Layered Hybrid Halide Perovskites. *J. Am. Chem. Soc.* **2022**, *144*, 1313−1322.
(18) Zhang, H.; Li, W.; Essman, J.; Quarti, C.; Metcalf, I.; Chiang, W.-Y.; Sidhik, S.; Hou, J.; Fehr, A.; Attar, A.; et al. Ultrafast Relaxation of Lattice Distortion in Two-Dimensional Perovskites. *Nat. Phys.* **2023**, *19*, 545−550.
(19) Nishida, J.; Breen, J. P.; Lindquist, K. P.; Umeyama, D.; Karunadasa, H. I.; Fayer, M. D. Dynamically Disordered Lattice in a Layered Pb-I-SCN Perovskite Thin Film Probed by Two-Dimensional Infrared Spectroscopy. *J. Am. Chem. Soc.* **2018**, *140*, 9882−9890.
(20) Xing, X.; Li, J.; Breen, J. P.; Nishida, J.; Karunadasa, H. I.; Fayer, M. D. Probing Lattice Dynamics in Two-Dimensional Inorganic Pseudohalide Perovskites with Ultrafast Infrared Spectroscopy. *J. Phys. Chem. C* **2022**, *126*, 10145−10158.
(21) Weadock, N. J.; Sterling, T. C.; Vigil, J. A.; Gold-Parker, A.; Smith, I. C.; Ahammed, B.; Krogstad, M. J.; Ye, F.; Voneshen, D.; Gehring, P. M.; et al. The Nature of Dynamic Local Order in $CH_3NH_3PbI_3$ and $CH_3NH_3PbBr_3$. *Joule* **2023**, *7*, 1051−1066.
(22) Hamm, P.; Zanni, M. T. *Concepts and Methods of 2D Infrared Spectroscopy*; Cambridge University Press: New York, 2012.
(23) Kwak, K.; Park, S.; Finkelstein, I. J.; Fayer, M. D. Frequency-Frequency Correlation Functions and Apodization in Two-Dimensional Infrared Vibrational Echo Spectroscopy: A New Approach. *J. Chem. Phys.* **2007**, *127*, 124503.
(24) Kwak, K.; Rosenfeld, D. E.; Chung, J. K.; Fayer, M. D. Solute-Solvent Complex Switching Dynamics of Chloroform between Acetone and Dimethylsulfoxide-Two-Dimensional IR Chemical Exchange Spectroscopy. *J. Phys. Chem. B* **2008**, *112*, 13906−13915.
(25) Hoffman, D. J.; Fayer, M. D. CLS Next Gen: Accurate Frequency−Frequency Correlation Functions from Center Line Slope Analysis of 2D Correlation Spectra Using Artificial Neural Networks. *J. Phys. Chem. A* **2020**, *124*, 5979−5992.
(26) Nishida, J.; Yan, C.; Fayer, M. D. Enhanced Nonlinear Spectroscopy for Monolayers and Thin Films in near-Brewster's Angle Reflection Pump-Probe Geometry. *J. Chem. Phys.* **2017**, *146*, No. 094201.
(27) Wu, B.; Breen, J. P.; Xing, X.; Fayer, M. D. Controlling the Dynamics of Ionic Liquid Thin Films Via Multilayer Surface Functionalization. *J. Am. Chem. Soc.* **2020**, *142*, 9482−9492.
(28) Tan, H.-S.; Piletic, I. R.; Fayer, M. Orientational Dynamics of Water Confined on a Nanometer Length Scale in Reverse Micelles. *J. Chem. Phys.* **2005**, *122*, 174501.
(29) Tokmakoff, A. Orientational Correlation Functions and Polarization Selectivity for Nonlinear Spectroscopy of Isotropic Media. II. Fifth Order. *J. Chem. Phys.* **1996**, *105*, 13−21.
(30) Sokolowsky, K. P.; Fayer, M. D. Dynamics in the Isotropic Phase of Nematogens Using 2D IR Vibrational Echo Measurements on Natural-Abundance ^{13}CN and Extended Lifetime Probes. *J. Phys. Chem. B* **2013**, *117*, 15060−15071.
(31) Rodgers, J. M.; Zhang, W.; Bazewicz, C. G.; Chen, J.; Brewer, S. H.; Gai, F. Kinetic Isotope Effect Provides Insight into the Vibrational Relaxation Mechanism of Aromatic Molecules: Application to Cyano-Phenylalanine. *J. Phys. Chem. Lett.* **2016**, *7*, 1281−1287.
(32) Kenkre, V. M.; Tokmakoff, A.; Fayer, M. D. Theory of Vibrational-Relaxation of Polyatomic-Molecules in Liquids. *J. Chem. Phys.* **1994**, *101*, 10618−10629.
(33) Jones, L. H. Infrared Spectrum and Structure of the Thiocyanate Ion. *J. Chem. Phys.* **1956**, *25*, 1069−1072.
(34) Nakamoto, K. Infrared and Raman Spectra of Inorganic and Coordination Compounds. In *Handbook of Vibrational Spectroscopy*; John Wiley & Sons, Ltd., 2006; p 1875.
(35) Beecher, A. N.; Semonin, O. E.; Skelton, J. M.; Frost, J. M.; Terban, M. W.; Zhai, H.; Alatas, A.; Owen, J. S.; Walsh, A.; Billinge, S. J. L. Direct Observation of Dynamic Symmetry Breaking above Room Temperature in Methylammonium Lead Iodide Perovskite. *ACS Energy Lett.* **2016**, *1*, 880−887.
(36) Lanigan-Atkins, T.; He, X.; Krogstad, M. J.; Pajerowski, D. M.; Abernathy, D. L.; Xu, G. N. M. N.; Xu, Z.; Chung, D. Y.; Kanatzidis, M. G.; Rosenkranz, S.; et al. Two-Dimensional Overdamped Fluctuations of the Soft Perovskite Lattice in $CsPbBr_3$. *Nat. Mater.* **2021**, *20*, 977−983.
(37) Nishida, J.; Fayer, M. D. Theory of Third-Order Spectroscopic Methods to Extract Detailed Molecular Orientational Dynamics for Planar Surfaces and Other Uniaxial Systems. *J. Chem. Phys.* **2014**, *140*, 144702.
(38) Nishida, J.; Yan, C.; Fayer, M. D. Orientational Dynamics of a Functionalized Alkyl Planar Monolayer Probed by Polarization-Selective Angle-Resolved Infrared Pump−Probe Spectroscopy. *J. Am. Chem. Soc.* **2016**, *138*, 14057−14065.
(39) Lipari, G.; Szabo, A. Model-Free Approach to the Interpretation of Nuclear Magnetic Resonance Relaxation in Macromolecules. 1. Theory and Range of Validity. *J. Am. Chem. Soc.* **1982**, *104*, 4546−4559.
(40) Lipari, G.; Szabo, A. Effect of Librational Motion on Fluorescence Depolarization and Nuclear Magnetic-Resonance Relaxation in Macromolecules and Membranes. *Biophys. J.* **1980**, *30*, 489−506.
(41) Wang, C. C.; Pecora, R. Time-Correlation Functions for Restricted Rotational Diffusion. *J. Chem. Phys.* **1980**, *72*, 5333−5340.
(42) Moilanen, D. E.; Fenn, E. E.; Lin, Y. S.; Skinner, J. L.; Bagchi, B.; Fayer, M. D. Water Inertial Reorientation: Hydrogen Bond Strength and the Angular Potential. *Proc. Natl. Acad. Sci. U. S. A.* **2008**, *105*, 5295−5300.
(43) Ramasesha, K.; Roberts, S. T.; Nicodemus, R. A.; Mandal, A.; Tokmakoff, A. Ultrafast 2D IR Anisotropy of Water Reveals Reorientation During Hydrogen-Bond Switching. *J. Chem. Phys.* **2011**, *135*, No. 054509.
(44) Kramer, P. L.; Giammanco, C. H.; Fayer, M. D. Dynamics of Water, Methanol, and Ethanol in a Room Temperature Ionic Liquid. *J. Chem. Phys.* **2015**, *142*, 212408.
(45) Fica-Contreras, S. M.; Charnay, A. P.; Pan, J.; Fayer, M. D. Rethinking Vibrational Stark Spectroscopy: Peak Shifts, Line Widths, and the Role of Non-Stark Solvent Coupling. *J. Phys. Chem. B* **2023**, *127*, 717−731.
(46) Skinner, J. L.; Hsu, D. Optical and Vibrational Dephasing in Crystals: Theory and Experiment. *J. Lumin.* **1987**, *38*, 134−136.
(47) Skinner, J. L.; Hsu, D. Vibrational Dephasing in Crystals: Theory and Experiment. *Chem. Phys.* **1988**, *128*, 35−45.

https://doi.org/10.1021/acs.jpcc.3c02251
J. Phys. Chem. C XXXX, XXX, XXX−XXX

(48) Skinner, J. L. Theory of Pure Dephasing in Crystals. *Annu. Rev. Phys. Chem.* **1988**, *39*, 463−478.
(49) Benson, S. W. Bond Energies. *J. Chem. Educ.* **1965**, *42*, 502−518.
(50) Kerr, J. A. Bond Dissociation Energies by Kinetic Methods. *Chem. Rev.* **1966**, *66*, 465−500.

https://doi.org/10.1021/acs.jpcc.3c02251
J. Phys. Chem. C XXXX, XXX, XXX−XXX